

Local-scale heterogeneity of photosynthetically active radiation (PAR), absorbed PAR and net radiation as a function of topography, sky conditions and leaf area index

Andrew Oliphant*, C. Susan, B. Grimmond, Hans-Peter Schmid, Craig A. Wayson

San Francisco State University, CA, USA

Received 1 July 2004; received in revised form 5 September 2005; accepted 17 September 2005

Abstract

The local-scale spatial distribution of photosynthetically active radiation (PAR), absorbed PAR (APAR) and net all-wave radiation (Q^*) across the top of a forest canopy was investigated as a function of topography, sky conditions and forest heterogeneity for a forested hilly study site located in south-central Indiana, USA that is part of the FLUXNET and SpecNet networks. The method to estimate spatial variability of radiation components utilized theoretical radiation modeling applied to a topographic model combined with spatial distribution of leaf area index derived from IKONOS imagery and empirical models derived from data collected on a single flux tower. Modeled PAR and Q^* compared consistently well with observations from a single tower with differences typically less than 10%, although clear-sky conditions were simulated more accurately than cloudy conditions. Spatial variability of radiation was found to be very sensitive to topographic relief and could be scaled linearly by mean slope angle. Decreases in optical transmissivity and increases in cloudiness had a strong effect of reducing both the spatial average and standard deviation of radiation components. Spatial variability of APAR was 53% greater than PAR and the characteristic scale of variance was reduced due to finer scale and magnitude of variance of LAI. Clear seasonal patterns existed in both spatial average and standard deviation values with summer producing the largest mean values and weakest spatial variability due to smaller solar zenith angles and seasonality in both optical transmissivity (scaled linearly by specific humidity) and cloudiness. These findings of spatial variability illustrate the need to characterize the complex landscape patterns at flux tower sites, particularly where the goal is to relate flux tower data to satellite imagery.

© 2006 Elsevier Inc. All rights reserved.

Keywords: Photosynthetically active radiation; Gross ecological production; Absorbed par

1. Introduction

Radiation fluxes at the Earth's surface play important roles in many ecological, climatological, and hydrological systems. Biological activity is strongly dependent on radiative transfer both directly, through the interaction between phytoelements and radiant energy emitted by the sun, and indirectly through micrometeorological controls. Understanding the spatial distribution of photosynthetically active radiation (PAR) is important for predicting patterns of ecosystem functioning within a forest (Vierling & Wessman, 2000) and gross ecological production (GEP) has been directly linked with PAR in numerous studies (e.g. Goulden et al., 1997; Gu et al., 1999; Monteith, 1972;

Oliphant et al., 2002; Schmid et al., 2000). Improvements in remote sensing technology and techniques to estimate photosynthetic activity using hyperspectral sensors can be used to assess small scale spatial variability of ecosystem dynamics (Blackburn, 1999; Gamon et al., 1993; Rahman et al., 2001, 2003). Net all-wave radiation provides the fundamental input to the surface energy balance and spatial variability has been linked with a variety of biometeorological controls including surface climates (Kalthoff et al., 1999) and rates of evapotranspiration (Famiglietti & Wood, 1995) as well as boundary layer processes and local thermal circulations (Kossmann et al., 2002). Since seasonality plays a critical role in temporal variability of ecosystem functioning, it is also important to observe the role of seasons on spatial variability of radiation due to changing geometric relations, optical transmissivity and cloud conditions.

* Corresponding author. Tel.: +1 415 405 2143; fax: +1 415 338 6243.
E-mail address: andrewo@sfsu.edu (A. Oliphant).

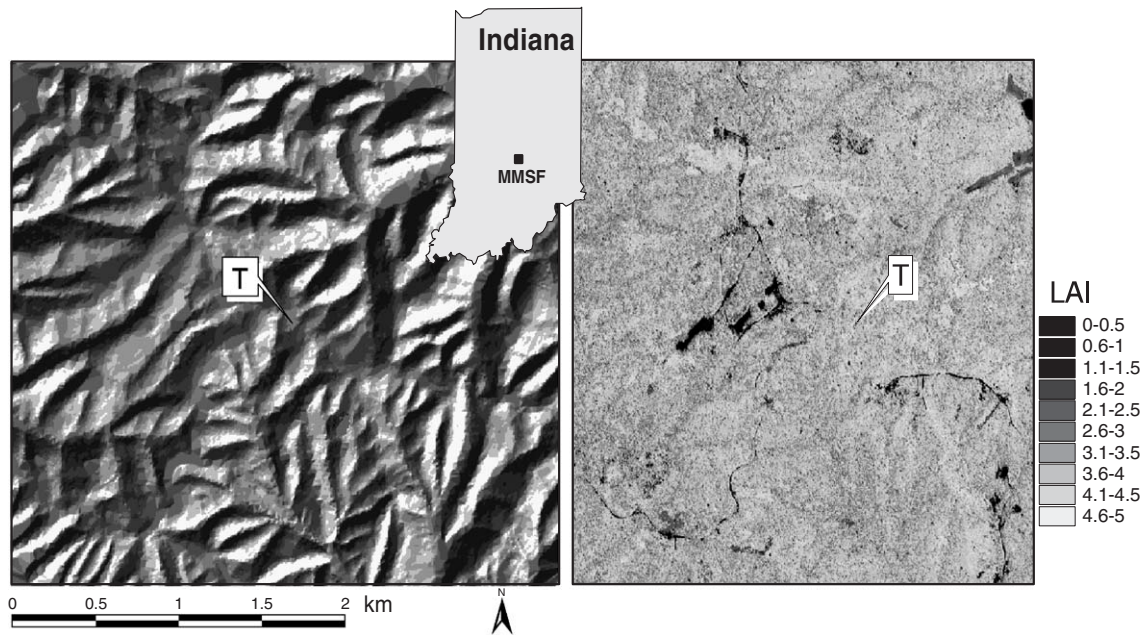


Fig. 1. Site map of the study area within the Morgan–Monroe State Forest, south-central Indiana, USA; shaded relief map (left) and LAI map (right) generated from IKONOS satellite imagery captured July 6, 2000. Elevation ranges from 192 m to 297 m. *T* indicates the location of the 46-m instrumented tower. Note, image has less coverage to the east of the tower than the topographic map.

Current theoretical models and satellite derived data can provide valuable insight into spatial variability of surface radiation fluxes (Diak et al., 2004; Dubayah et al., 1990; Dubayah & Loebel, 1997; McKenney et al., 1999; Oliphant et al., 2003). Here we explore the use of theoretical models of surface radiation fluxes in complex topography, IKONOS imagery (visible and near-infrared) and empirical relations determined from data collected from a single flux tower to estimate components of spatial variability of (PAR), absorbed PAR (APAR) and net all-wave radiation (Q^*) for a forested hilly region of mid-western USA. The primary objective is to estimate local-scale spatial heterogeneity of radiative fluxes at the *top* of the forest canopy across a topographically complex area. In particular we examine the role of topography, forest heterogeneity, optical transmissivity, cloud cover and seasonality on spatial variability of radiation.

Combining ecosystem modeling, satellite image interpretation and point observations has greatly enhanced the spatial understanding of ecosystem–atmosphere interaction at the continental to global scale (Running et al., 1999), although there remains a need to improve understanding of small-scale variability to inform downscaling of regional or larger models. Furthermore, characterization of ecosystem–atmosphere inter-

action is often based on data collected at individual towers using the eddy covariance approach (e.g. Schmid et al., 2000) as well as optical sampling techniques (Gamon et al. this issue). Assessing the spatial distribution of radiation components is therefore an important step toward scaling up of point measurements to regional-scale ecosystem estimates and variability within the source areas of turbulent flux measurements.

2. Site description and observational data

The location for this research was the Morgan–Monroe State Forest (MMSF) in south-central Indiana, mid-western USA (39°19'N, 86°25'W). MMSF is an extensive managed forest with a total area of 95.3 km² (Schmid et al., 2000). The area used for model and image analysis in this study is a 3.5 × 3.5 km area of near-contiguous forest cover. At the center of this area on a ridge top with unobstructed sky view, is a 46-m instrumented AmeriFlux tower. Fig. 1 shows the shaded relief within the study area and the leaf area index (LAI) estimated from an IKONOS satellite image captured July 6, 2000 (4 m pixel size), using the empirical conversion from the normalized difference vegetation index (NDVI) described by Wulder et al. (1998); $LAI = 17.35 \times NDVI - 9.01$. The spatial average LAI

Table 1
Instrumentation used in the present study and factory estimates of accuracy

Variable	Height	Manufacturer	Model	Accuracy
$K\downarrow, K\uparrow$	46 m	Kipp and Zonen, Delft, The Netherlands	CM3	±10% (daily sums)
$L\downarrow, L\uparrow$	46 m	Kipp and Zonen, Delft, The Netherlands	CG3	±10% (daily sums)
PAR	46 m	Licor, Lincoln, NE	LI190	±2% (per year)
Air temperature	46 m	Vaisala, Sunnyvale, CA	HMP35C	±0.4 °C
Relative humidity	46 m	Vaisala, Sunnyvale, CA	HMP35C	±3%
Atmos. pressure	Surface	Vaisala, Sunnyvale, CA	PTA 427	±4 hPa (−20–45 °C)

estimated for the study area is $3.4 \text{ m}^2 \text{ m}^{-2}$, while the spatial standard deviation is $0.85 \text{ m}^2 \text{ m}^{-2}$. Values in the vicinity of the tower are $4\text{--}4.5 \text{ m}^2 \text{ m}^{-2}$, which compare closely with mid-summer observations using a leaf area index meter (LAI-2000, LiCor Inc, Lincoln Nebraska as reported in Oliphant et al.

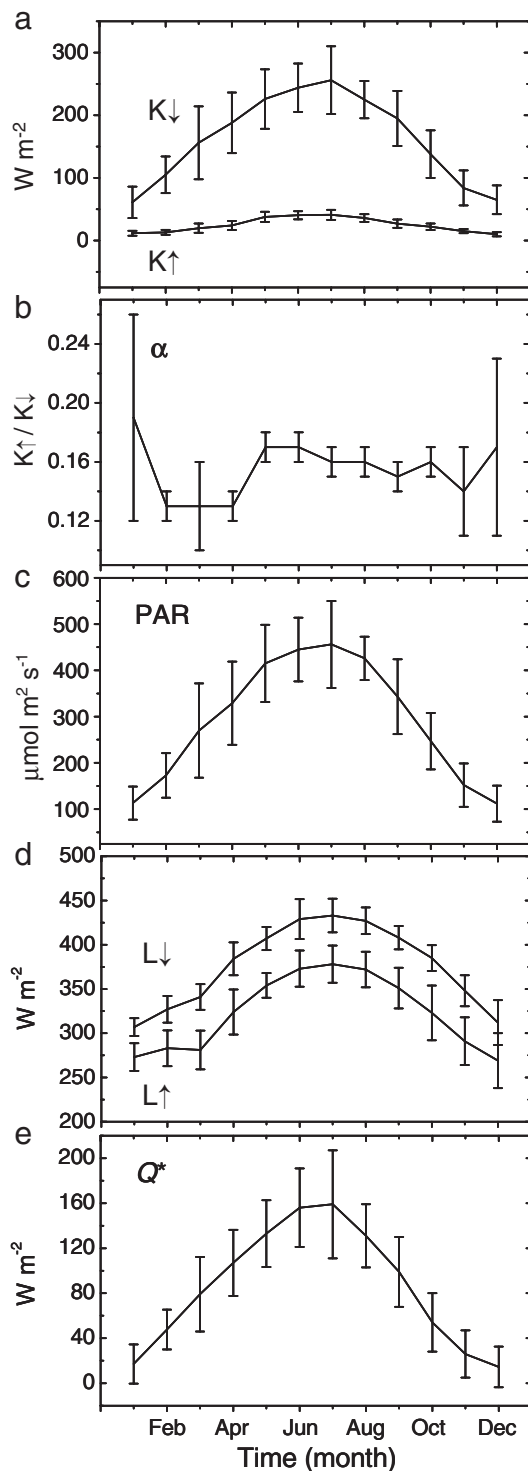


Fig. 2. Monthly mean and standard deviation of diurnal mean radiation flux densities from 46 m on the MMSF tower, March 1998 to December 2001, a) shortwave radiation ($K\downarrow$, $K\uparrow$), b) albedo, c) longwave radiation ($L\downarrow$, $L\uparrow$), d) Photosynthetically active radiation (PAR), e) net all-wave radiation (Q^*).

(2004). The area has a ridge-ravine topography with a relative relief of $<60 \text{ m}$, and an overall elevation range of $<100 \text{ m}$. Mean slope angle within the study area (Fig. 1) is 10.6° , estimated from a digital elevation model (DEM) at 5 m resolution. Slope aspect is fairly randomly distributed but with a slight general southerly orientation. The MMSF is composed of secondary successional broadleaf forest within the maple–beech to oak–hickory transition zone of the eastern deciduous forest, with a mean canopy height of $25\text{--}27 \text{ m}$. The forest is comprised predominantly of sugar maple (*Acer saccharum*, 27%), tulip poplar (*Liriodendron Tulipifera*, 19%), sassafras (*Sassafras albidum*, 9.5%), white oak (*Quercus alba*, 9%), and black oak (*Quercus nigra*, 8.5%). A more detailed breakdown of species composition is given in Ehman et al. (2002).

The tower (see Fig. 1) is used for flux measurements of CO_2 , heat, water vapor and radiation as part of the AmeriFlux and FLUXNET observational networks as well as general meteorological variables (Schmid et al., 2000). This site is also part of the SpecNet network, where remote sensing is systematically applied and linked to eddy covariance data (e.g. Rahman et al., 2004) for an improved understanding of controls on surface-atmosphere fluxes. In this study, radiation data from March 1998 to December 2000 from the 46 m level are used for empirical parameterization of the model, while data from January 2000 to December 2001 are used to assess the model's climatological representation of seasonal and inter-annual variability. The radiation components measured at that level include incoming (\downarrow) and outgoing (\uparrow) short (K) and long (L) wave radiation (in W m^{-2}) and incoming PAR (in quantum units of $\mu\text{mol m}^{-2} \text{ s}^{-1}$). Instrumentation details are provided in Table 1.

By way of introducing the seasonal context for this study, monthly mean and standard deviation of diurnal mean radiation fluxes and albedo, based on data from March 1998 to December 2001, are presented in Fig. 2. Strong seasonality can be seen in each of the variables. For $K\downarrow$, $K\uparrow$ and PAR, the importance of solar declination for this mid-latitude site is evident, while the large annual range in $L\downarrow$ and $L\uparrow$ indicate the continental influence of the location on air and surface temperature. The influence of foliage on the radiation budget is evident in the seasonal albedo pattern. Albedo abruptly increases with emergence of leaves in spring and then steadily declines as the foliage darkens throughout the summer. The effect of snow falls, particularly in December and January can also be seen to increase both monthly mean and variability of albedo. The intra-monthly variability of radiation components is significant and varies seasonally, suggesting the importance of cloudiness and synoptic changes throughout the year. In sum however, Q^* shows a reasonably consistent increase in temporal variability toward the summer months when mean values are largest.

3. Spatial model description

Surface radiation modeling in complex terrain has received growing attention in recent decades, although many studies have tended to focus on individual components, primarily incident shortwave radiation (Dubayah et al., 1990; Dubayah & Rich, 1995; Dubayah & van Katwijk, 1992; Kumar et al., 1997; Olseth

& Skartveit, 2001; Whiteman, 1990; Whiteman & Allwine, 1986) or net shortwave radiation (Dubayah & Loechel, 1997), but including longwave radiation (Marks & Dozier, 1979), and PAR (Olseth & Skartveit, 1997), as well as the complete radiation budget (Gallant, 1997; McKenny et al., 1999; Nunez, 1980; Oliphant et al., 2003; Wang et al., 2002). The surface radiation model used in this study is based on calculations of K_{\downarrow} , PAR, and fluxes of longwave radiation across a surface generated by a DEM, using sun–Earth geometric relations and parameters derived empirically from tower data. Additionally, APAR is derived from modeled PAR and summertime leaf area index determined from IKONOS satellite imagery (Fig. 1). Alados and Alados-Arboledas (1999) suggested that closed stands of plants can be treated as inclined surfaces receiving the global irradiance corresponding to the surface inclination. This assumes that canopy height is uniform across the landscape and leaf orientation reflects that of the surface. Based on visual observations of the forest from above, it is clear that the canopy surface generally follows the topographic surface, although the mixed forest produces individual tree height variability that adds additional ‘topographic’ heterogeneity at a smaller scale (~10 m). This effect, not accounted for in the current study, is expected to be small for average radiation fluxes at the scale of local topography, although implies underestimation in our calculation of spatial variability.

3.1. Global solar radiation

Initially, extraterrestrial shortwave irradiance on a horizontal surface just outside the Earth’s atmosphere (K_{oh}) is calculated as a function of the solar constant (1367 W m^{-2}), latitude, time of year and hour angle, based on the formulae of Kondratyev (1977). Incident direct beam shortwave radiation on a horizontal plane at the Earth’s surface (K_{Sh}) as well as the diffuse beam component (K_D) which is irrespective of slope angle is then calculated using:

$$K_{Sh} = K_{oh} \tau^m \quad (1)$$

and

$$K_D = (0.271 - 0.294 \tau^m) K_{oh} \quad (2)$$

where τ is the transmission coefficient or fraction of radiation incident at the top of the atmosphere which reaches the Earth’s surface along the vertical path and m is the ratio of the path length in the direction of the sun at zenith angle (z) to the path length in the vertical direction and is given by $m = \sec z = 1 / \cos z$ (Gates, 1980; Linacre, 1992). Since the curvature of the Earth unrealistically inflates m when z is less than about 60° , values in this range are taken from List (1968). The derivation of τ is discussed in Section 3.2.

K_D was then divided between 5° circumsolar (K_{Dc}) and isotropic (K_{Di}) fractions of K_D , using a circumsolar coefficient (γ) of 0.25 after Linacre (1992) so that $K_{Dc} = K_D \gamma$ and $K_{Di} = K_D (1 - \gamma)$. A sky view factor (ψ_s) is calculated for each grid point using the one-dimensional horizon algorithm of Dozier et al.

(1981) and K_{Di} is reduced by a factor of $1 - \psi_s$. K_{Dc} and K_S are then calculated for sloping surfaces using the cosine law:

$$K_S = K_{Sh} \cos i \quad (3)$$

where i is the angle between the solar beam and normal to the sloping surface. This can be derived from:

$$\cos i = \cos s \cos z + \sin s \sin z \cos(A - A_s) \quad (4)$$

where s is the slope angle, A is the solar azimuth angle and A_s the azimuth angle of the slope. The grid points with and without shading (both self shading and shading from surrounding terrain) at each interval were then determined and K_S and K_{Dc} were removed from shaded grid points. The contribution of reflected shortwave radiation (K_r) arriving at each grid point was also determined using:

$$K_r = (K_S + K_D)(1 - \psi_s) \alpha \quad (5)$$

where α is albedo, derived from monthly average observations at the tower. Albedo is assumed to be isotropic in calculating this component. The total shortwave radiation (K_{TS}) for clear skies was calculated from:

$$K_{TS} = K_{Dc} + K_{Di} + K_S + K_r. \quad (6)$$

These calculations were performed across the spatial domain at 3° hour-angle (12-minute) intervals from sunrise to sunset.

3.2. Optical transmissivity and cloudiness

Reduction in atmospheric clarity is caused by absorption, reflection and scattering of solar radiation by gases, particulates and water droplets along the atmospheric path. The first two are often considered together in the form of the optical transmission coefficient, and change relatively little over shorter time scales of hours to days (Wilson & Gallant, 2000), while the third identifies the importance of cloudiness which can have dramatic control over radiative transfer on the time scale of minutes to hours (Gu et al., 2001). In this study, we estimate the clear-sky optical transmission coefficient and cloud controls separately.

The transmission coefficient (τ) was estimated for each daylight hour using all clear sky days by:

$$\tau = \left[\frac{K_{Sho}}{K_{oh}} \right]^{\frac{1}{m}} \quad (7)$$

where K_{Sho} is the observed shortwave radiation received at a horizontal surface (on tower). Fig. 3a shows the seasonal trend of τ with lowest values occurring in summer months and highest in winter and Fig. 3b shows that the seasonal variability in τ is negatively correlated with specific humidity (q) at 46 m on the tower. The annual range of monthly mean τ is 0.11, which impacts both the total amount of solar radiation reaching the surface and the ratio of K_D to K_S which also impacts the spatial variability (Eqs. (1) and (2)). For the MMSF case, seasonal variability of τ can be largely accounted for by q using relatively simple empirical models (Fig. 3b). However, although q contributes to τ , it cannot be concluded that it is the dominant

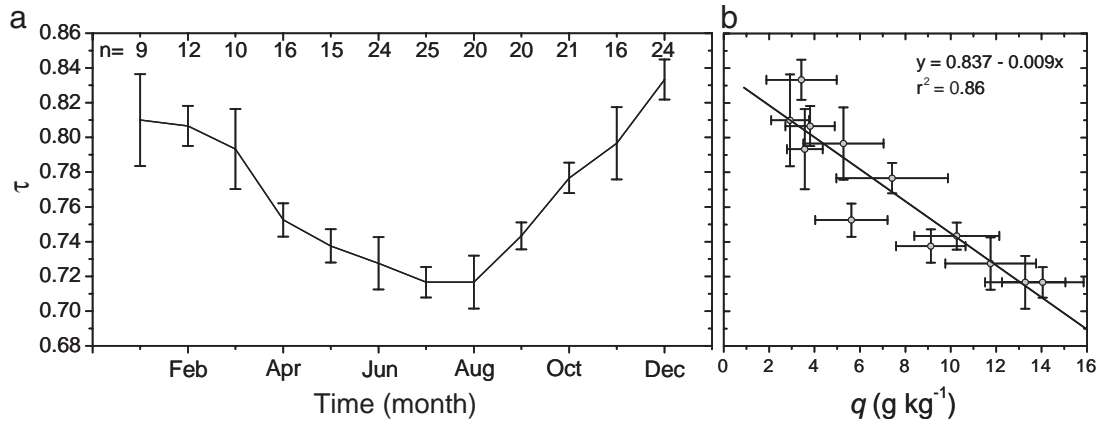


Fig. 3. Monthly mean and standard deviation of diurnal mean optical transmissivity (τ), a) over the annual cycle and b) as a function of monthly mean and standard deviation of daily mean specific humidity (q) at 46 m. Vertical error bars show standard deviation of τ , horizontal bars show standard deviation of q . Data include all available complete clear-sky days (n = number of days in sample) from March 1998 to December 2001.

cause since, for example, summertime high levels of q coincides with high temperatures and levels of UV, both precursors to ozone production, which also reduces τ .

In order to identify the effect of clouds on $K\downarrow$ accurately, many properties of the sky cover are required, including cloud cover area, location in the sky with respect to the sun, cloud density, cloud height, and cloud type. Since these properties are not known in detail for this site and are difficult to determine accurately, a simple cloudiness index (k_c) is used. k_c has been determined for a variety of applications including assessing variability in net ecosystem exchange based on attenuation of solar radiation (Gu et al., 1999) and longer term climate change analyses using thermal infrared radiation (Marty, 2000), which has the advantage of providing nocturnal values. Since we are interested in the role of clouds on solar radiation, we use a simple index based on the difference between observed and modeled clear-sky irradiance for each hour of the observation period using:

$$k_c = \frac{K_{\text{Sho}}}{K_{\text{TS}}} \quad (8)$$

where, K_{Sho} and K_{TS} are the observed total shortwave radiation incident on a horizontal surface and modeled for the same surface point and time but under clear-sky conditions respectively. From hourly values of k_c , monthly statistics of clear-sky fraction (θ) and cloud transmittance (β) were calculated. The θ fraction is the ratio of the hours where $k_c \approx 1$ to the total number of daylight hours for each day. Because of small differences between modeled and observed clear sky values (K_{TS} and K_{Sho}), the criteria for clear skies used was $k_c = 1 \pm 0.05$. β is the mean daylight value of k_c , when $k_c < 1$, in other words, the fraction of potential clear sky radiation received in cloudy conditions. Daylight hours were determined by extracting values when solar zenith angle was less than 80° to avoid cosine response problems with the instruments at low solar angles. Monthly mean values of these two ratios are presented in Fig. 4. The clear-sky fraction shows a clear seasonal trend with largest frequency of cloudiness occurring in spring and summer months. Cloud transmittance shows a smaller seasonal range and a less consistent pattern

although, with the exception of June, a small increase in mean cloud transmission occurs during summer and autumn months.

The two cloud ratios are implemented in the model following the calculation of diurnal mean shortwave radiation for each grid point. Daily-integrated radiation values are combined with the associated θ and β coefficients using:

$$\bar{K}_{\text{TS}} = (\bar{K}_{\text{S}} + \bar{K}_{\text{D}})(\theta + (1-\theta)\beta_s) + \bar{K}_{\text{r}} \quad (9)$$

where the overbar indicates daily-integrated values and β_s is a modified form of β . Since diffuse radiation is enhanced under cloudy conditions, β is reduced to account for ψ_s , and increased to account for the enhanced flux of diffuse radiation received on shaded slopes, as shown empirically by Kondratyev (1969). This is approximated by Wilson and Gallant (2000):

$$\beta_s = \beta \psi_s \left(\frac{K_{\text{tsns}}}{K_{\text{tss}}} \right) \quad (10)$$

where K_{tsns} is the daily total clear sky shortwave radiation without shading and K_{tss} is the total daily clear sky shortwave radiation with shading.

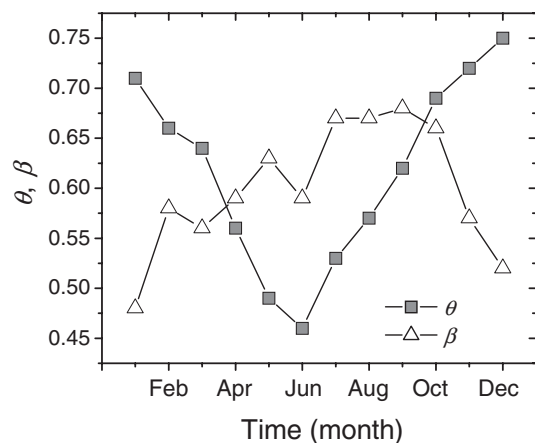


Fig. 4. Mean monthly clear-sky fraction (θ) and cloud transmittance (β) calculated from data collected at 46 m on the MMSF tower, March 1998 to December 2001.

Since the cloudiness parameterization is explicit over neither space nor time on shorter intervals than a day, this approach is only useful for longer-term statistical assessments of the control of cloudiness and where preferential location for the development of clouds is negligible. In this study locational consistency for cloud formation is thought to be minimal, since both topography and surface properties within the region are reasonably homogenous. However, differences in cloud type occur throughout the year at this site, with summer months typically producing more spatially heterogeneous cumuliform cloud while in winter, stratiform cloud is more commonly observed.

3.3. PAR and APAR

Numerous studies have identified a near constant relation between $K\downarrow$ and PAR, regardless of sky conditions (Howell et al., 1983; Rao, 1984). More detailed investigations have highlighted differences in the ratio of diffuse beam PAR to K_D (Alados & Alados-Arboledas, 1999; Grant et al., 1996). Alados et al. (1996) analyzed the relation between PAR and $K\downarrow$ for a variety of sky condition variables, including clearness indices, solar zenith angle and dew point temperature. From this, they derived statistically robust models to estimate this ratio using multiple regression of sky condition variables. However, the models were found to weaken only slightly when only simple clearness indices were used.

In this study, we define the relation between observed $K\downarrow$ and PAR for a range of sky conditions using k_c (Eq. (8)). k_c was binned into five 0.2 categories between 0 and 1 and the relations between $K\downarrow$ and PAR were derived for each (Fig. 5). Overall relatively small change in the mean ratio occurred as a function of clearness (0.19), although showed an increase of slope with clearness, as also found by Alados et al. (1996) for a site in central Spain. In this case, increase of the slope as a function of k_c followed a logarithmic curve ($s_{(PAR/K\downarrow)} = 0.089 \ln(k_c) + 1.821$) with an r^2 of 0.987. Further, it is clear that, while consistency is very good for each k_c bin, it improves with increasing k_c , showing that increased cloudiness weakens confidence in the model. Fortunately, this pattern is inverse to the frequency (n) with which these conditions occur.

In order to assess the effect of spatial variability of radiation on potential photosynthetic rates, it is necessary to consider the spatial distribution of leaf density across the model domain. The spatial distribution of LAI for the study area estimated from IKONOS imagery (Fig. 1) and provides a basis for calculating the fraction of PAR that is absorbed (FPAR) using an exponential function based on Beer’s law (Baret & Guyot, 1991):

$$FPAR = P_\infty [1 - \exp(-LAI)] \tag{11}$$

where P_∞ is the asymptotically limiting value of PAR absorption for an infinitely thick canopy and was set to 0.94 (Wiegand & Hatfield, 1988). This assumes that the leaves are randomly distributed. FPAR is then multiplied by modeled incoming PAR to derive absorbed photosynthetically active radiation (APAR).

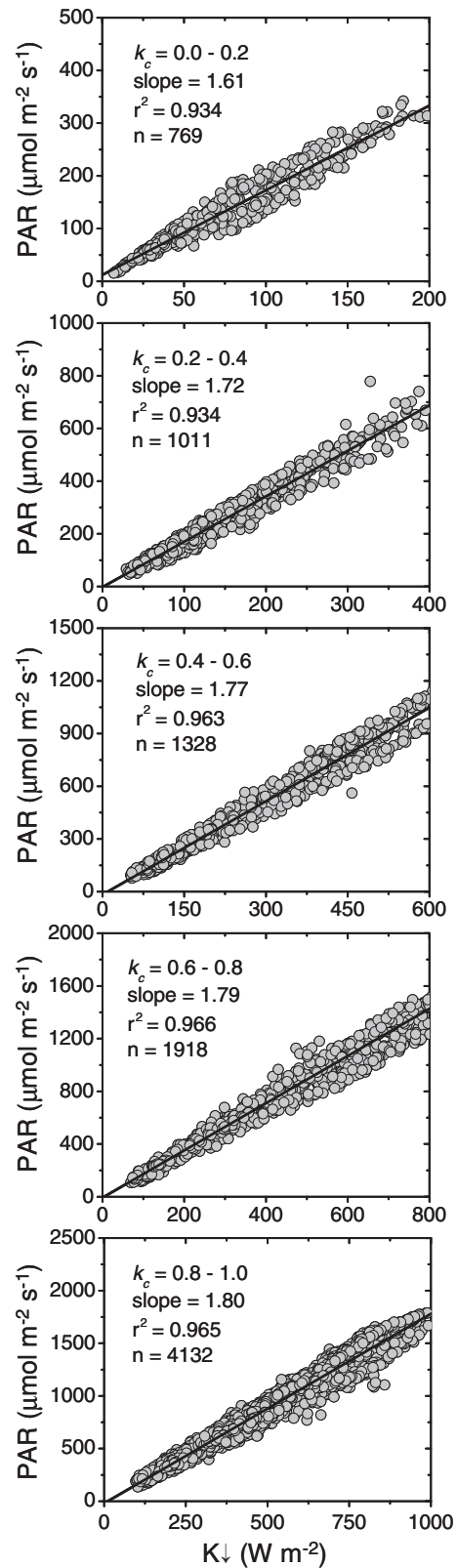


Fig. 5. The relation between PAR and $K\downarrow$ for five different cloudiness index k_c bins (Eq. (10)) observed at 46 m on the MMSF tower, March 1998 to December 2001, where slope is the slope of the least squares regression, r^2 is the coefficient of determination and n is the sample size (number of hours). Note, axes are scaled differently but maintain the same aspect ratio.

3.4. Net all-wave radiation

Daily values of Q^* are calculated using;

$$Q^* = K_{TS} - (1 - \alpha)K_{TS} + L\downarrow - L\uparrow \quad (12)$$

where α is the daily albedo, $L\uparrow$ is upwelling longwave radiation from observations on the tower and $L\downarrow$ is calculated from;

$$L\downarrow = L\downarrow_{(obs)}\psi_s + (1 - \psi_s)L\uparrow_{(obs)} \quad (13)$$

where ψ_s (sky view factor) is used to determine the ratio of $L\downarrow$ received from sky to surrounding terrain. Therefore, the variability of longwave components across space is restricted to variability of ψ_s . Oliphant et al. (2003) showed that for a very topographically complex alpine location, spatial variability in net longwave radiation (L^*) contributed very little to the overall spatial variability of Q^* and that the greatest contribution to this variability was due to changes in elevation, followed by changes in the ratio of $L\downarrow$ received from sky to surrounding terrain, as a function of ψ_s . In the current study, we assume that elevation has a negligible control on spatial variability since the range in elevation is < 100 m (2% of the range in the study area of Oliphant et al. (2003)) and we have no way of accurately determining a lapse rate at 46 m across the terrain.

3.5. Model evaluation

Since the model is applied to assess variability of radiation components where observational data do not exist, we are inherently restricted from being able to test the model's ability to predict changes across space in this study. However, Oliphant et al. (2003) evaluated the performance of the solar radiation formulations used here (Eqs. (1)–(6)) using observations collected within an alpine basin and reported a root mean squared error (RMSE) of 31.7 W m^{-2} for K_{TS} , 37.8 W m^{-2} for K_S and 7.2 W m^{-2} for K_D (less than 15% of mean), with r^2 values above 0.97.

In this case it is at least possible to compare modeled radiation values with the single tower observations in order to test the model's ability to capture the seasonal cycle and effects of clouds. Simulations of mean monthly radiation components were conducted with τ , α , θ , and β derived from observational data collected during 1998 and 1999 and the results were compared with observational data from 2000 and 2001. Comparisons include mean monthly values and visually determined clear sky days within each month. Table 2 shows that all components are reproduced well by the model through the seasonal cycle, particularly for clear-sky days, with a small overestimation by the model. The root mean squared error (RMSE) is in all cases less than 10% of the mean value. For clear-sky cases, the dominant portion of RMSE is unsystematic (RMSE_U), suggesting that interannual differences in empirical inputs are likely to account for larger error than systematic (RMSE_S) errors by the model. For the mean monthly simulations which incorporate cloud effects, error is more evenly spread between RMSE_U and RMSE_S, indicating that inter-annual differences in cloudiness generated as much error as systematic weaknesses in capturing the reduction and diffusion of solar

Table 2

Statistical results of the comparison between modeled and observed monthly mean radiation flux densities at the location of the MMSF tower for 2000 and 2001, where Slope and Intercept are for linear least squares regression, RMSE is the root mean squared error, subscript _S refers to the systematic portion of error and _U to the unsystematic portion and the sample size is 24 (months)

	$K\downarrow$	$K\uparrow$	$L\downarrow$	$L\uparrow$	Q^*	PAR
<i>All-sky</i>						
r^2	0.985	0.971	0.882	0.948	0.984	0.988
Slope	0.95	0.97	0.89	0.83	0.90	0.87
Intercept	18.66	2.51	36.2	59.98	15.88	35.73
RMSE	12.88	2.56	14.66	14.62	10.84	21.23
RMSE _S	10.46	1.82	4.87	10.37	9.05	17.41
RMSE _U	7.50	1.81	13.83	10.30	5.96	12.14
Mean Diff ($\pm\%$)	9.46	10.62	0.04	-0.98	29.9	2.64
<i>Clear-sky</i>						
r^2	0.985	0.969	0.961	0.935	0.980	0.953
Slope	0.97	0.90	0.97	0.96	0.95	0.96
Intercept	9.7	3.46	8.59	12.97	10.33	18.27
RMSE	10.72	2.87	9.48	12.84	10.30	31.97
RMSE _S	4.14	1.52	1.86	1.97	5.50	6.14
RMSE _U	9.87	2.44	9.30	12.69	8.71	31.38
Mean Diff ($\pm\%$)	2.02	2.24	0.58	-0.09	7.41	0.93

Units for Intercept, RMSE, RMSE_S and RMSE_U are, for $K\downarrow$, $K\uparrow$, $L\downarrow$, $L\uparrow$ and Q^* , W m^{-2} and for PAR, $\mu\text{mol m}^{-2} \text{ s}^{-1}$.

radiation by clouds. Finally, since solar incident angle strongly influences surface radiation fluxes and varies equally widely across space and time, it follows that the performance of the model through time will be indicative of its performance across space, at least with respect to the role of solar incident angle.

4. Results

This section reports on spatial variability of radiation fluxes found as a function of topography, cloudiness, seasonality and surface heterogeneity. For this analysis, simulations included empirical inputs from data collected from 1998 to 2001.

4.1. Spatial variability of fluxes

Two sets of daily simulations were run for a single generic year for this site using 5 m resolution grid points, differing only in cloudiness parameters. In the first, θ and β were parameterized by the k_c analysis (Section 3.2). In the second, both of these parameters were set to 1, in order to simulate equivalent clear-sky days. From these two simulation sets, annual, growing season and monthly mean values of spatial mean and standard deviation of radiation flux densities were compiled. Growing season was evaluated from three years of phenological data, with an average start day of April 9 and stop day of October 30 and length of 204 days.

The spatial distribution of growing season mean PAR and annual mean Q^* are shown in Fig. 6. The upper maps show the distribution of grid point values for observed cloudiness parameters, clearly showing the effects of topography, with larger values found on south-facing slopes. The lower maps show the difference between equivalent clear sky simulations and observed sky simulations (clear sky–observed sky). These show the

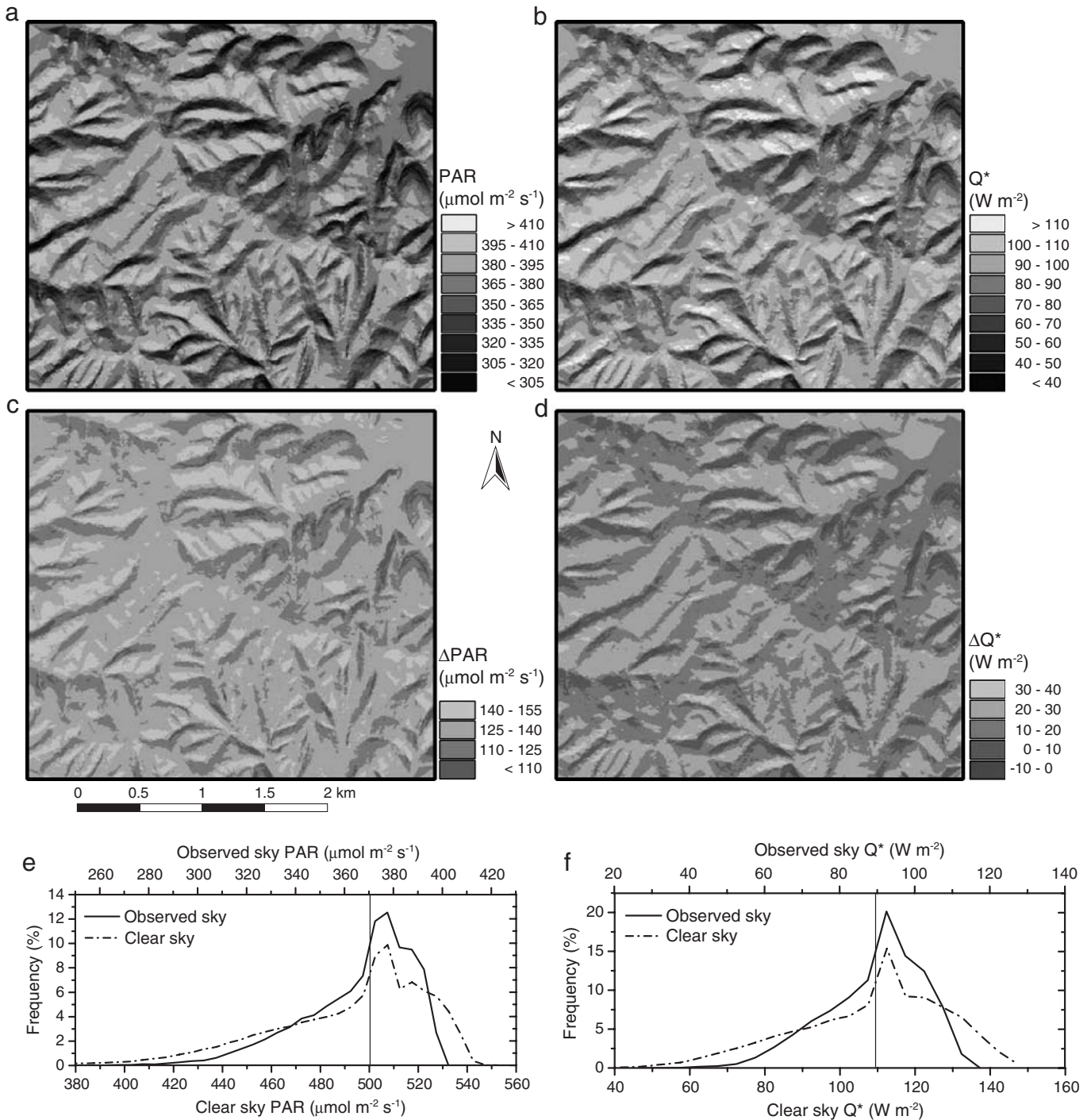


Fig. 6. Maps of model output for a) annual mean PAR using observed sky conditions, b) growing season mean Q^* using observed sky conditions, c) difference between clear sky and observed sky PAR, d) difference between clear sky and observed sky Q^* and frequency histograms of grid point values for both clear and observed sky for e) PAR, f) Q^* . Note horizontal scales on histograms have been translated so that spatial average values (vertical lines) are aligned.

enhancement of both spatial mean and variability of fluxes under clear sky, than observed sky conditions. Similar spatial patterns exist for both PAR and Q^* . Frequency histograms of grid point values for both radiation components under both sky conditions plotted relative to their spatial means clearly indicates the role of cloudiness in reducing the variance found in grid points across the model domain. Peaks in the histograms reflect the large number of grid points with near-zero slope angle.

The overall spatial variability for both fluxes is considerable. For Q^* , the spatial standard deviation for the year under observed cloudiness is 13.2 W m^{-2} , which is 15% of the mean, while the overall range is 77.3 W m^{-2} (86% of mean). As an annual energy total this integrates to $2775 \pm 416.3 \text{ MJ m}^{-2} \text{ a}^{-1}$ (with the \pm value being one spatial standard deviation) and a range of $2439 \text{ MJ m}^{-2} \text{ a}^{-1}$. In the case of PAR over the growing season, the spatial standard deviation for observed cloudiness is

23.7 $\mu\text{mol m}^{-2} \text{s}^{-1}$, 6.4% of the mean, while the range is 93.8 (25% of mean). This integrates over the growing season to 9336 \pm 597.5 mol m^{-2} .

4.2. Role of topography

Spatial variability of solar radiation within localized areas has been found to be dominated by slope angle and aspect (Dubayah et al., 1990; Oliphant et al., 2003). Consequently, scales of local relief strongly impact the magnitude of variability found in a given region. Since relief is a function of scale, spatial resolution in topographic models provides a proxy for varying levels of topographic relief or complexity. Modeling radiation using different spatial resolutions can be used as a tool to assess spatial variability of radiation as a function of topographic complexity. Dubayah et al. (1990) and McKenney et al. (1999) examined the role of topographic resolution on solar radiation and reported very little change in spatial mean values but large changes in spatial variability. Dubayah (1991) showed theoretically that spatial variability of solar radiation across a topographically complex area can be scaled by the mean slope angle. To examine the role of DEM resolution in this study, simulations were run for a clear-sky summer day using identical meteorological parameters, but varying DEM resolution; 5, 20, 50, 100, 200 and 500 m, with grid-point counts of 490,000, 30,625, 4900, 1225, 306 and 49 respectively.

The spatial standard deviation of PAR and Q^* as a function of DEM resolution is presented in Fig. 7a. Spatial variability, in both cases, follows an exponential decay as DEM resolution decreases linearly. Spatial mean and standard deviation of slope angles were also calculated for each DEM resolution and follow a similar exponential decay pattern. Therefore, spatial variability of radiation fluxes in this case shows a strong positive linear correlation with both spatial mean and standard deviation of slope angle (Fig. 7b and c respectively). Dubayah (1991) showed theoretically that this scaling of radiation variance was linked only with mean slope and that radiation variance is not changed when variance in slope angle is reduced to zero, as long as slope aspect is uniformly distributed. The resulting linear equations for the relation between radiation variability and mean slope angle (\bar{s}) are $\sigma_{\text{PAR}} = 1.5 + 6.6\bar{s}$ and $\sigma_{Q^*} = 1.76 + 1.9\bar{s}$, where σ refers to the spatial standard deviation and the overbar refers to the spatial mean. The r^2 value for both relations was greater than 0.997. The magnitude of decrease in spatial variability between 5 and 500 m resolution models for PAR_σ is 60% and Q^*_σ is 71%. Spatial average radiation fluxes should remain similar at each resolution, in order to satisfy the conservation of energy (Dubayah et al., 1990). However, in this case, a small increase of 2% in the spatial average occurs between 5 and 500 m resolution for both PAR and Q^* , probably due to the reduction of shaded area from surrounding terrain in smoother topography.

4.3. Role of cloudiness

Comparing model output for observed cloudiness with equivalent clear-sky conditions (Fig. 6), spatial average PAR is

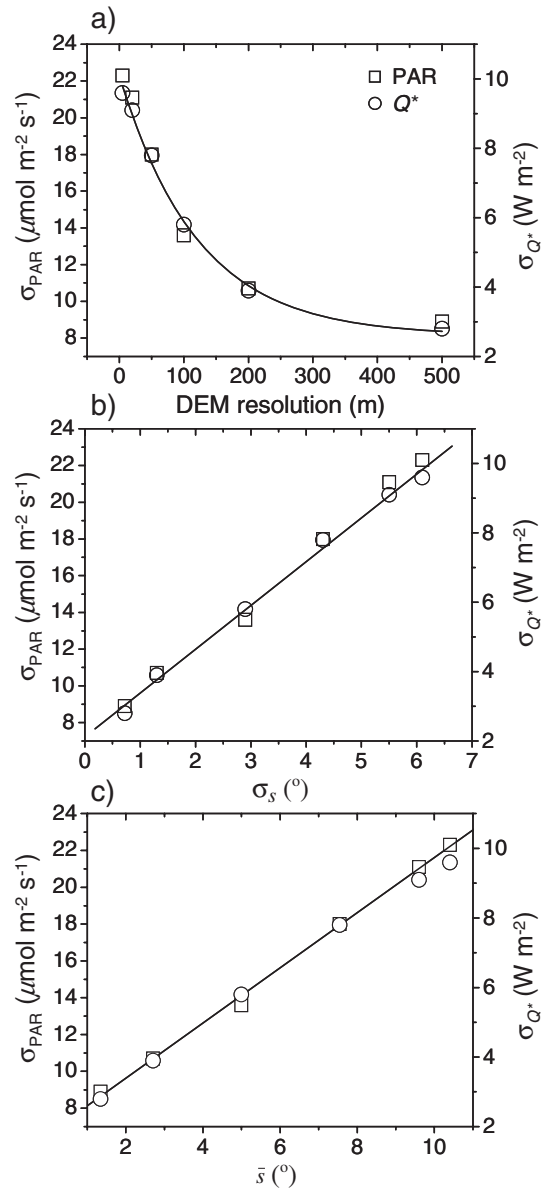


Fig. 7. Spatial standard deviation of PAR and Q^* as a function of a) DEM resolution, b) spatial standard deviation slope angle and c) spatial mean slope angle for the simulation of July 15.

reduced by 36% with a reduction in spatial standard deviation of 20%. Q^* also showed a lower spatial mean for the observed sky conditions than for equivalent clear-sky conditions (reduction of 17%), as well as a smaller standard deviation (reduction of 36%). The smaller reduction in mean Q^* is accounted for by the larger input of $L\downarrow$ during cloudy conditions, which partly offsets the reduction in incident solar radiation. Furthermore, the larger reduction in spatial variability of Q^* than PAR, indicates the spatial uniformity of $L\downarrow$ compared with $K\downarrow$, and the role of clouds to increase the ratio of K_D to K_S .

The role of cloudiness on spatial variability was assessed by simulating a single day in mid summer (July 15) under 25 different cloudiness scenarios using a range of θ and β coefficients from 0.2 to 1.0, at increments of 0.2 and determining spatial standard deviation for each run (Fig. 8).

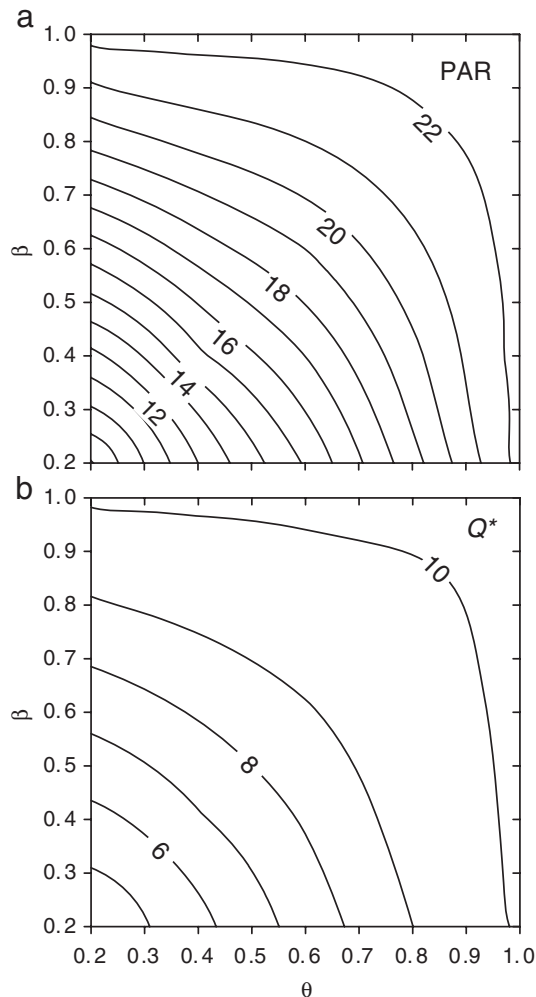


Fig. 8. Contour plots of spatial standard deviation of a) PAR ($\mu\text{mol m}^{-2} \text{s}^{-1}$) and b) Q^* (W m^{-2}) as a function of changes in θ and β modeled for July 15 at this site.

For both PAR and Q^* , the spatial standard deviation reduces evenly with decreases in both θ and β parameters, indicating equivalent controls of both the clear-sky fraction and cloud transmittance. The similarity of pattern in the two plots further indicates the dominance of solar radiation in controlling the spatial variability of Q^* . In both cases, the reduction of direct beam solar radiation as a function of cloudiness clearly has a large impact on reducing spatial variability.

4.4. Role of forest heterogeneity

Fig. 9 shows average growing season APAR calculated using the methods described in Section 3.3. The effect of gaps in the canopy due to roads, lakes and parking areas can clearly be seen to affect the spatial distribution of APAR as well as the topographical effects on PAR as observed in Fig. 6. The spatial growing season average APAR is $330 \mu\text{mol m}^{-2} \text{s}^{-1}$ and the spatial standard deviation is $41.4 \mu\text{mol m}^{-2} \text{s}^{-1}$ which integrates to $5837 \pm 729.7 \text{ mol m}^{-2}$ for the growing season. The overall fraction of PAR that is absorbed for the study area is

0.89 while the spatial standard deviation of APAR is 53% higher than PAR. This is an important difference when APAR is considered as a driver of ecosystem functioning through the light response curve. For example, using the Schmid et al. (2000) non-linear relation between PAR and Gross Ecosystem Production (GEP) applied to a) the spatial growing season average modeled PAR and b) discretely to each grid point of modeled growing season average PAR and then spatially averaging the resultant, produces a difference in GEP of $0.2 \text{ t C ha}^{-1} \text{ a}^{-1}$ (1.5%). Furthermore, it produces a spatial standard deviation of $3.4 \text{ t C ha}^{-1} \text{ a}^{-1}$ across the model domain, which is 25% of the annual total calculated for a single growing season at the MMSF tower (Schmid et al., 2000). This simplistic approach does not account for spatial variability of other environmental constraints such as turbulence characteristics, vapor pressure deficit, soil moisture content and temperature but provides a potential spatial variability of mean GEP as a function of the non-linearity of the light response curve. It also ignores the fact that the estimates of GEP are already integrated across the footprint for the flux measurements. Further work is currently underway to examine the relation between the footprint integrated flux and the ecosystem integrated flux in relation to both normalized difference vegetation index and APAR. Preliminary results (Schmid et al., 2002) show that the flux footprint is usually large enough to spatially average LAI induced variability to within about 2%, but not large enough to average over several topographical elements that influence the distribution of PAR or APAR. The increased use of high spatial and spectral frequency optical observations such as those discussed in Gamon et al. (this issue) should greatly enhance spatial interpretation and up-scaling of turbulent flux measurements.

4.5. Seasonal trends in spatial variability

In order to establish the seasonal context for spatial distribution of radiation components, integrated monthly values

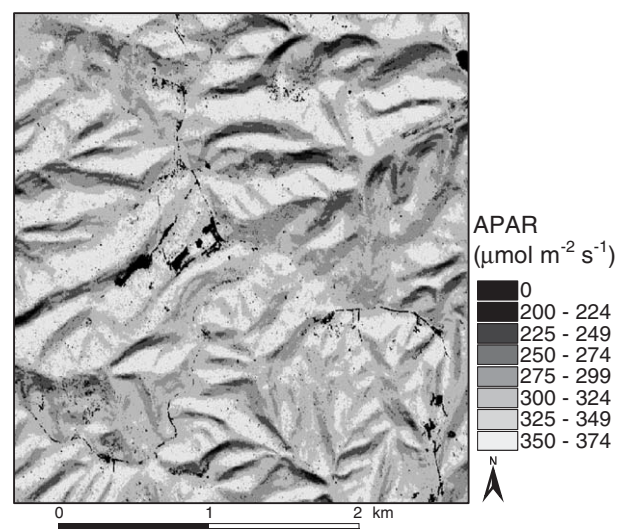


Fig. 9. Growing season average absorbed photosynthetically active radiation (APAR) for the MMSF study area. Note break in scale between 0 (roads, lakes and clearings) and $200 \mu\text{mol m}^{-2} \text{s}^{-1}$.

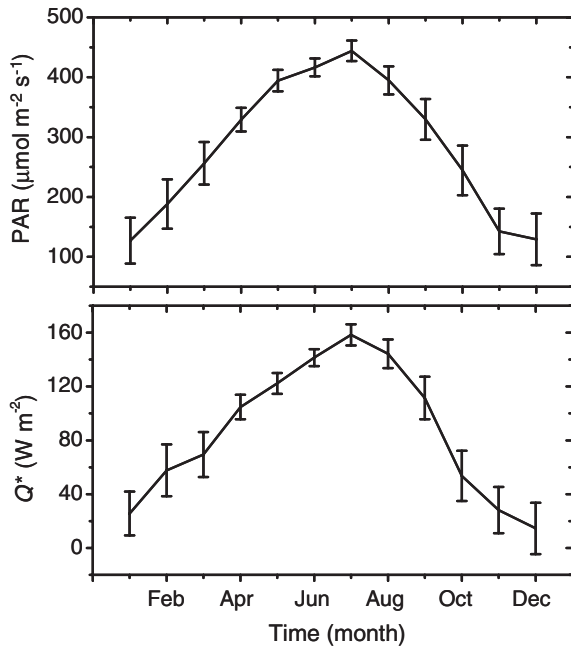


Fig. 10. Modeled monthly spatial mean radiation flux densities with spatial standard deviation bars for PAR and Q^* under observed sky conditions.

were calculated for observed sky conditions (Fig. 10). The seasonal trend for the mean and standard deviation are negatively correlated, with the larger mean values and smaller variability found during summer than winter months. As a result, monthly mean spatial standard deviation of Q^* ranges from 6.3 W m^{-2} in June to 19.2 W m^{-2} in February. Monthly spatial standard deviation of PAR ranges from $14.8 \text{ } \mu\text{mol m}^{-2} \text{ s}^{-1}$ in June to $43.1 \text{ } \mu\text{mol m}^{-2} \text{ s}^{-1}$ in December. Both of these trends are a function of the seasonal change in solar declination, as was also found by Dubayah et al. (1990) for clear sky solar radiation over the Konza Prairie, Kansas as well as increases in cloudiness in summer (Fig. 4). The implication for annual budgets is that overall spatial variability is diminished by the weighting of summertime values. Furthermore, spatial variability is smallest when the influence of Q^* on evapotranspiration and PAR on photosynthesis is greatest, during the growing season. The non-linear relation between PAR and GEP tends to saturate at higher levels of PAR (e.g. Schmid et al., 2000) adding a level of spatial smoothing during midday summer hours.

4.6. Semi-variance analysis

The features of semi-variograms, particularly the range, provide a useful measure to compare the characteristic scale of derived radiation fields with the environmental controls that drive them (Dubayah, 1991). Isotropic semi-variograms were calculated from all pairings of values extracted from 300 randomly located points within grids of slope angle, slope aspect, LAI and modeled radiation fields, using the formulations of Oliver (1990). The sample size of randomly generated points was selected after comparing histograms from a range of sample sizes with that of the original 5 m grids. A sample

of 300 points was determined to represent the overall distribution well, while being relatively quick to compute the semi-variograms (approximately 45,000 pairs). Semi-variograms from four different sets of 300 randomly generated points were also compared and model parameters were found to vary by less than 4%. For this analysis the same 300 points were used to extract samples from the 5 m resolution grids and 40×25 m lags were used to compute the semi-variogram. Comparisons were made with semi-variograms using 20×50 m and 100×10 m lags and similar results were produced. Only the LAI grid produced a significant nugget which was dominated by microscale variation, indicating spatial structure at scales smaller than captured here (Oliver, 1990). An exponential model of the form $\gamma(h) = C(1 - e^{-h/r})$ was fit to the data, where $\gamma(h)$ is the semi-variance at a distance (h), C is the sill variance, and r a distance parameter related to the range (Dubayah, 1991).

The semi-variograms produced from slope angle and aspect, LAI, Q^* , PAR and APAR all showed similar exponential form and ranges, although the sill variance and RMSE of model fit varied considerably (Table 3). Slope angle and LAI have the smallest characteristic scale with slope aspect the largest. The PAR and Q^* model grids produce similar ranges which lie between the ranges of the topographic attributes (slope angle and aspect) that principally control them. Since the parameterization of cloud effects is the same across all grid cells in this study, the scale of radiation variance is not affected, although there is a strong reduction in the magnitude. The semi-variogram of APAR clearly reflects both the underlying topography and vegetation, whereby the range lies between incident PAR and LAI, and the increase in the sill variance of APAR from PAR is provided by LAI, as reported earlier (using standard deviation).

In general, the heterogeneity of several landscape properties relevant to radiation incidence and absorption represented at 5 m resolution showed similar characteristic scales although with significantly different variances. The impact of these scales on radiation distribution is also clearly evident. Furthermore, the range produced from semi-variograms of radiation fields increased when input DEM resolution was increased. This

Table 3

Features of semi-variograms calculated from all pairings of 300 point values from randomly generated locations within the grids of listed variables

Variable	Unit	Range (m)	Sill (unit^2)	RMSE (unit)
Slope angle	degrees	116	43.3	7.1
Slope aspect	degrees	145	9538	97.7
LAI	$\text{m}^2 \text{ m}^{-2}$	116	0.31	0.53
Growing season PAR	$\mu\text{mol m}^{-2} \text{ s}^{-1}$	135	452	21.2
Growing season PAR (clear)	$\mu\text{mol m}^{-2} \text{ s}^{-1}$	134	873	29.8
APAR	$\mu\text{mol m}^{-2} \text{ s}^{-1}$	122	622	24.7
Annual average Q^*	W m^{-2}	137	163	13.0
Annual average Q^* (clear)	W m^{-2}	137	394	20.1

Lag size = 25 m, number of lags = 40, Range is the distance (m) at which variance saturates and Sill is the variance at saturation. RMSE is the root mean square error of the exponential model fit to each semi-variogram.

implies that under-representing the heterogeneity of the landscape in radiation modeling or simple up-scaling of point measurements unrealistically diminishes the overall variability and increases the characteristic distance scale of heterogeneity. It also implies the need for more detailed spatial investigations of heterogeneity of landscape properties, including remotely sensed estimates of biophysical functioning.

5. Conclusions

Potential spatial variability of PAR and Q^* were investigated for a hilly mid-latitude forested region in southern Indiana, in order to identify the relative controls of local scale topography, forest heterogeneity and atmospheric conditions. Simulations were run for observed cloudiness as well as the equivalent clear-sky conditions. Monthly mean model output compared well with observed point data with differences typically less than 10% and clear-sky days were simulated more accurately than cloudy days, although this was restricted to a single point in space.

Spatial variability of radiation was found to be very sensitive to topographic relief, while spatial mean changed only slightly. This was due to a reduction in mean slope angle, and shows that reduction in model resolution may not adversely affect spatial aggregate values, but will significantly underestimate the spatial variability, although the topographic component can be scaled linearly by mean slope. Clouds reduced both spatial mean and standard deviation of radiation components significantly, with the spatial mean Q^* reduction being less than PAR, and the reduction in the standard deviation greater. The spatial variability of APAR was 53% higher than PAR indicating the importance of variance in FPAR provided by heterogeneity of the leaf area index. Strong seasonal patterns in both spatial mean and standard deviation were evident, with summer having the largest mean and smallest variability. Seasonal patterns of spatial variability were driven by changing geometric relations, optical transmissivity and cloud conditions.

Additional local-scale heterogeneity of soil and atmospheric characteristics not assessed in this study would provide a more complete picture of spatial variability of ecosystem and functioning and climate. Results also imply that finer spatial resolution LAI data used in this study is required to more accurately characterize the spatial scales of vegetation. Further work is also required to evaluate this potential variability from observations and add vertical integration of APAR for deep canopies. Nevertheless, topographic radiation models combined with satellite imagery and empirical relations (both location dependent and independent) can yield valuable information on the spatial distribution and variance of radiation components. The magnitude and patterns of radiation variability at this scale are important for both upscaling of point flux tower or optical sampling data as well as downscaling of regional or larger models or assessing sub-pixel variability. These findings also imply the need for more detailed investigations of heterogeneity of landscape properties to better understand spatial variability of ecosystem functioning, particularly through the use of remotely sensed biophysical variables.

List of Symbols and Abbreviations

A	Solar azimuth angle (degrees)
A_s	Slope azimuth angle (degrees)
APAR	Absorbed photosynthetically active radiation ($\mu\text{mol m}^{-2} \text{s}^{-1}$)
α	Albedo (0–1 ratio)
β	Ratio of radiation transmittance through clouds (0–1 ratio)
β_s	Modified form of β (0–1 ratio)
FPAR	Fraction of absorbed photosynthetically active radiation (0–1 ratio)
γ	Circumsolar coefficient (0–1 ratio)
GEP	Gross ecological production ($\mu\text{mol m}^{-2} \text{s}^{-1}$)
i	Angle of solar beam relative to nadir (degrees)
K	Shortwave (solar) radiation (W m^{-2})
k_c	Cloud index (0–1 ratio)
K_D	Diffuse beam shortwave radiation (W m^{-2})
K_{Dc}	Circumsolar fraction of diffuse beam shortwave radiation (W m^{-2})
K_{Di}	Isotropic fraction of diffuse beam shortwave radiation (W m^{-2})
K_{oh}	Shortwave irradiance on a surface-parallel plane (W m^{-2})
K_r	Incident shortwave radiation reflected from terrain (W m^{-2})
K_S	Direct beam shortwave radiation on a sloping surface (W m^{-2})
K_{Sh}	Direct beam shortwave radiation on a horizontal surface (W m^{-2})
K_{Sho}	Observed radiation on a horizontal surface (W m^{-2})
K_{TS}	Total shortwave radiation for clear skies (W m^{-2})
K_{tsns}	Daily total clear sky shortwave radiation without shading (W m^{-2})
K_{tss}	Daily clear sky shortwave radiation with shading (W m^{-2})
L	Longwave (thermal infrared) radiation (W m^{-2})
LAI	Leaf area index ($\text{m}^2 \text{m}^{-2}$)
m	Airmass (radiative pathlength relative to nadir) ($1-\infty$ ratio)
P_∞	Asymptotically limiting value of PAR absorption (0–1 ratio)
PAR	Photosynthetically active radiation ($\mu\text{mol m}^{-2} \text{s}^{-1}$)
q	Specific humidity (g kg^{-1})
Q^*	Net all-wave radiation (W m^{-2})
s	Slope angle (degrees)
τ	Optical transmissivity (at nadir) (0–1 ratio)
θ	Fraction of clear sky hours (0–1 ratio)
ψ_s	Sky view factor (0–1 ratio)
z	Solar zenith angle (degrees)

Acknowledgements

Funding for this research was provided by NIGEC, Dept. of Energy (Co-operative Agreement No. DE-FC03-90ER61010). The authors would like to thank the large number of people involved in data collection at the MMSF tower site, particularly Steve Scott and Brian Offerle.

References

- Alados, I., & Alados-Arboledas, L. (1999). Direct and diffuse photosynthetically active radiation: Measurements and modeling. *Agricultural and Forest Meteorology*, *93*, 27–38.
- Alados, I., Foyo-Moreno, I., & Alados-Arboledas, L. (1996). Photosynthetically active radiation: Measurements and modeling. *Agricultural and Forest Meteorology*, *78*, 121–131.
- Baret, F., & Guyot, G. (1991). Potentials and limits of vegetation indices for LAI and APAR assessment. *Remote Sensing of Environment*, *35*, 161–173.
- Blackburn, G. A. (1999). Relationships between spectral reflectance and pigment concentrations in stacks of deciduous broadleaves. *Remote Sensing of Environment*, *70*, 224–237.
- Diak, G. R., Mecikalski, J. R., Anderson, M. C., & Norman, J. M. (2004). Estimating land surface energy budgets from space: Review and Current Efforts at the University of Wisconsin–Madison and USDA–ARS. *Bulletin of the American Meteorological Society*, *85*, 65–78.
- Dozier, J., Bruno, J., & Downey, P. (1981). A faster solution to the horizon problem. *Computers & Geosciences*, *7*, 145–151.
- Dubayah, R. (1991). *The topographic variability of solar radiation*. Unpublished PhD dissertation, Department of Geography, University of California, Santa Barbara, No. 9204596.
- Dubayah, R., Dozier, J., & Davis, F. W. (1990). Topographic distribution of clear-sky radiation over the Konza Prairie, Kansas, USA. *Water Resources Research*, *26*, 679–690.
- Dubayah, R., & Loechel, S. (1997). Modeling topographic solar radiation using GOES data. *Journal of Applied Meteorology*, *36*, 141–154.
- Dubayah, R., & Rich, P. M. (1995). Topographic solar radiation models for GIS. *International Journal of Geographical Information Systems*, *9*, 405–419.
- Dubayah, R., & van Katwijk, V. (1992). The topographic distribution of annual incoming solar radiation in the Rio Grande River basin. *Geophysical Research Letters*, *19*, 2231–2234.
- Ehman, J. L., Schmid, H. P., Grimmond, C. S. B., Randolph, J. C., Hanson, P. J., Wayson, C. A., et al. (2002). An initial intercomparison of micrometeorological and ecological inventory estimates of carbon exchange in a mid-latitude deciduous forest. *Global Change Biology*, *8*, 575–589.
- Famiglietti, J. S., & Wood, E. F. (1995). Effects of spatial variability and scale on areally averaged evapotranspiration. *Water Resources Research*, *31*, 699–712.
- Gallant, J. C. (1997). Modeling solar radiation in forests of southeastern Australia. *Proceedings of International Congress on Modeling and Simulation (MOD-SIM97)*, Hobart, Tasmania, December 1997 (pp. 575–579).
- Gamon, J. A., Field, C. B., Roberts, D. A., Ustin, S. L., & Valentini, R. (1993). Functional patterns in an annual grassland during an AVIRIS overflight. *Remote Sensing of Environment*, *44*, 1–15.
- Gates, D. M. (1980). *Biophysical ecology*. New York: Springer-Verlag. 611 pp.
- Goulden, M. L., Daube, B. C., Fan, S.-M., Sutton, D. J., Bazzaz, A., Munger, J. W., et al. (1997). Physiological responses of a black spruce forest to weather. *Journal of Geophysical Research*, *102*, 28,987–28,996.
- Grant, R. H., Heisler, G. M., & Gao, W. (1996). Photosynthetically-active radiation: Sky radiance distributions under clear and overcast conditions. *Agricultural and Forest Meteorology*, *82*, 267–292.
- Gu, L., Fuentes, J. D., Garstang, M., da Silva, J. T., Heitz, R., Sigler, J., et al. (2001). Cloud modulation of surface solar irradiance at a pasture site in southern Brazil. *Agricultural and Forest Meteorology*, *106*, 117–129.
- Gu, L., Fuentes, J. D., & Shugart, H. H. (1999). Responses of net ecosystem exchanges of carbon dioxide to changes in cloudiness: Results from two North American deciduous forests. *Journal of Geophysical Research*, *104*, 31421–31434.
- Howell, T. A., Meek, D. W., & Hatfield, J. L. (1983). Relationship of photosynthetically active radiation to shortwave radiation in the San Joaquin Valley. *Agricultural Meteorology*, *28*, 157–175.
- Kalthoff, N., Fiedler, F., Kohler, M., Kolle, O., Mayer, H., & Wenzel, A. (1999). Analysis of energy balance components as a function of orography and land use and comparison of results with the distribution of variables influencing local climate. *Theoretical and Applied Climatology*, *62*, 65–84.
- Kondratyev, K. Y. (1969). *Radiation in the atmosphere*. New York: Academic Press. 912 pp.
- Kondratyev, K. Y. (1977). *Radiation regime of inclined surfaces. Technical Note No. 152, WMO No. 467*. Geneva, Switzerland: World Meteorological Society. 129 pp.
- Kossmann, M., Sturman, A. P., Zawar-Reza, P., McGowan, H. A., Oliphant, A. J., Owens, I. F., et al. (2002). Analysis of the wind field and the heat budget in an alpine lake basin under summertime fair weather conditions. *Meteorology and Atmospheric Physics*, *81*, 27–52.
- Kumar, L., Skidmore, A. K., & Knowles, E. (1997). Modeling topographic variation in solar radiation in a GIS environment. *International Journal of Geographical Information Science*, *11*, 475–497.
- Linacre, E. T. (1992). Data-sparse estimation of lake evaporation, using a simplified penman equation. *Agricultural and Forest Meteorology*, *64*, 237–256.
- List, R. J. (Ed.). (1968). *Smithsonian Meteorological Tables*, 6th rev. ed. Washington, D.C.: Smithsonian Institution. 352 pp.
- Marks, D., & Dozier, J. (1979). A clear-sky longwave radiation model for remote Alpine areas. *Archiv für Meteorologie, Geophysik und Bioklimatologie. Serie B, Allgemeine und Biologische Klimatologie*, *27*, 159–187.
- Marty, C. (2000). *Surface radiation, cloud forcing and greenhouse effect in the Alps*. Unpublished PhD thesis, ETH, Zürich; 141 S:III [003897100].
- McKenny, D. W., Mackey, B. G., & Zavitz, B. L. (1999). Calibration and sensitivity analysis of a spatially distributed solar radiation model. *International Journal of Geographical Information Science*, *57*, 329–355.
- Monteith, J. L. (1972). Solar radiation and productivity in tropical ecosystems. *Journal of Applied Ecology*, *9*, 747–766.
- Nunez, M. (1980). The calculation of solar and net radiation in mountainous terrain. *Journal of Biogeography*, *7*, 173–186.
- Oliphant, A. J., Grimmond, C. S. B., Schmid, H. P., Su, H. -B., Scott, S. L., & Vogel, C. (2002, May). The role of cloud cover in net ecosystem exchange of CO₂ over two mid-western mixed hardwood forests. *Proceedings of 25th Conference on Agricultural and Forest Meteorology, Norfolk, VA*.
- Oliphant, A. J., Grimmond, C. S. B., Zutter, H. N., Schmid, H. P., Su, H. -B., Scott, S. L., et al. (2004). Heat storage and energy balance fluxes for a temperate deciduous forest. *Agricultural and Forest Meteorology*, *126*, 185–201.
- Oliphant, A. J., Spronken-Smith, R. A., & Sturman, A. P. (2003). Spatial variability of surface radiation fluxes in mountainous terrain. *Journal of Applied Meteorology*, *42*, 113–118.
- Oliver, M. A. (1990). Kriging: A method of interpolation for Geographical Information Systems. *International Journal of Geographical Information Science*, *4*, 313–332.
- Olseth, J. A., & Skartveit, A. (1997). Spatial distribution of photosynthetically active radiation over complex topography. *Agricultural and Forest Meteorology*, *86*, 205–214.
- Olseth, J. A., & Skartveit, A. (2001). Solar irradiance, sunshine duration and daylight illuminance derived from METEOSAT data for some European sites. *Theoretical and Applied Climatology*, *69*, 239–252.
- Rahman, A. F., Cordova, V. D., Gamon, J. A., Schmid, H. P., & Sims, D. A. (2004). Potential of MODIS ocean bands for estimating CO₂ flux from terrestrial vegetation: A novel approach. *Geophysical Research Letters*, *31*, L10503.
- Rahman, A. F., Gamon, J. A., Fuentes, D. A., Roberts, D. A., & Prentiss, D. (2001). Modeling spatially distributed ecosystem flux of boreal forests using hyperspectral indices from AVIRIS imagery. *Journal of Geophysical Research*, *106*(D24), 33,579–33,591.
- Rahman, A. F., Gamon, J. A., Sims, D. A., & Schmidts, M. (2003). Optimal pixel size for hyperspectral remote sensing of ecosystem function: A case study of Southern California Grassland and Chaparral. *Remote Sensing of Environment*, *84*, 192–207.
- Rao, C. R. (1984). Photosynthetically active components of global solar radiation: Measurements and model computations. *Archives for Meteorology, Geophysics, and Bioclimatology*, *33*, 89–98.
- Running, S. W., Baldocchi, D. D., Turner, D. P., Gower, S. T., Bakwin, P. S., & Hibbard, K. A. (1999, Oct). A global terrestrial monitoring network

- integrating tower fluxes, flask sampling, ecosystem modeling and EOS satellite data. *Remote Sensing of Environment*, 70, 108–127.
- Schmid, H. P., Grimmond, C. S. B., Cropley, F., Offerle, B., & Su, H. -B. (2000). Measurements of CO₂ and energy fluxes over a mixed hardwood forest in the mid-western United States. *Agricultural and Forest Meteorology*, 103, 357–374.
- Schmid, H. P., Oliphant, A. J., Wayson, C. A., & Randolph, J. C. (2002, May). An assessment of the spatial variability of biophysical factors near a CO₂ flux tower in a deciduous forest and its influence on annual estimates of net ecosystem exchange. Preprints 25th Conference Agriculture and Forest Meteorology, Norfolk, Virginia.
- Wang, S., Chen, W. J., & Cihlar, J. (2002). New calculation methods of diurnal distribution of solar radiation and its interception by canopy over complex terrain. *Ecological Modelling*, 155, 191–204.
- Whiteman, C. D. (1990). Observations of thermally developed wind systems in mountainous terrain. In W. Blumen (Ed.), *Chapter 2 in Atmospheric Processes Over Complex Terrain Meteor. Monogr.*, vol. 23 (no. 45) (pp. 5–42). Boston, Massachusetts: Amer. Meteor. Soc.
- Whiteman, C. D., & Allwine, K. J. (1986). Extraterrestrial solar radiation on inclined surfaces. *Environmental Software*, 1, 164–169.
- Wiegand, C. L., & Hatfield, J. L. (1988, July 1–10). The spectral agronomic Multi-site-multicrop Analyses (SAMMA). *Proc. 16th Cong., Int. Soc. Photogramm and Remote Sens., Kyoto, Japan*.
- Wilson, J. P., & Gallant, J. C. (2000). Secondary attributes. In J. P. Wilson, & J. C. Gallant (Eds.), *Terrain analysis: Principles and applications* (pp. 87–131). New York: John Wiley and sons.
- Wulder, M. A., LeDrew, E. F., Franklin, S. E., & Lavigne, M. B. (1998). Aerial image texture information in the estimation of northern deciduous and mixed wood forest leaf area index (LAI). *Remote Sensing of Environment*, 64, 64–76.
- Vierling, L. A., & Wessman, C. A. (2000). Photosynthetically active radiation heterogeneity within a monodominant Congolese rain forest canopy. *Agricultural and Forest Meteorology*, 103, 265–278.